SCIENCE CHINA
Physics, Mechanics & Astronomy

•Article•
Special Topic: Advances in Pulsed Laser Synthesis of Nanoparticles in Liquids

July 2022 Vol. 65 No. 7: 274206
https://doi.org/10.1007/s11433-021-1881-8

Computational study of laser fragmentation in liquid: Phase explosion, inverse Leidenfrost effect at the nanoscale, and evaporation in a nanobubble

Hao Huang[1,2], and Leonid V. Zhigilei[2*]

[1] *School of Mechanical Science and Engineering, Huazhong University of Science and Technology, Wuhan 430074, China;*
[2] *Department of Materials Science and Engineering, University of Virginia, Charlottesville 22904-4745, USA*

Received December 11, 2021; accepted February 28, 2022; published online May 25, 2022

Laser fragmentation in liquid is an effective and environment-friendly processing technique capable of yielding colloidal nanoparticles and atomic clusters with a narrow size distribution. The advancement of this technique can be facilitated by an improved understanding of processes that control the sizes, shapes, and structures of the produced nanoparticles. In this work, the dependence of the fragmentation mechanisms on the energy density deposited by the laser pulse is investigated in atomistic simulations performed for 20 nm Au nanoparticles irradiated in water by 10 ps laser pulses. The simulations reveal that the decrease in the absorbed laser energy leads to sequential transitions from the regime of "strong" phase explosion, when all products of an explosive phase decomposition of the irradiated nanoparticle are promptly injected into the water surrounding a nanobubble formed around the nanoparticle, to two distinct regimes of nanoparticle fragmentation leading to the formation of a large central nanoparticle surrounded by smaller satellite fragments. First, in the regime of "mild" phase explosion, the central nanoparticle is produced by the reflection of some of the hot metal droplets generated by the explosive decomposition of the nanoparticle from the boundary of the nanobubble. This reflection is attributed to the inverse Leidenfrost effect acting at the nanoscale. The reflected droplets converge in the center of the nanobubble and coalesce into a single droplet that solidifies shortly after the collapse of the nanobubble. Further decrease in the absorbed laser energy brings the irradiation conditions below the threshold for the phase explosion and results in the formation of a core-satellite structure of the fragmentation products through an interplay of the intense evaporation from the surface of the irradiated nanoparticle, evolution of the nanobubble, and condensation of the metal vapor into clusters and small satellite nanoparticles. The computational predictions are related to the experimental observations, and the connections between the fragmentation mechanisms, the nanoparticle size distribution, and the generation of internal crystal defects are discussed.

laser fragmentation in liquid, molecular dynamics simulations, phase explosion, inverse Leidenfrost effect, nanobubble, nanoparticles

PACS number(s): 81.07.-b, 05.70.Ln, 47.55.dp, 02.70.Ns, 47.11.Mn

Citation: H. Huang, and L. V. Zhigilei, Computational study of laser fragmentation in liquid: Phase explosion, inverse Leidenfrost effect at the nanoscale, and evaporation in a nanobubble, Sci. China-Phys. Mech. Astron. **65**, 274206 (2022), https://doi.org/10.1007/s11433-021-1881-8

1 Introduction

The rapidly growing utilization of nanoparticles in a broad range of applications [1,2] defines the need for accelerated development of advanced nanoparticle synthesis techniques capable of meeting the sharp rise in global demand [3]. Some of the applications, particularly in the fields of biomedicine [4-6] and catalysis [7-9], place stringent requirements on the

*Corresponding author (email: lz2n@virginia.edu)

quality and size uniformity of the nanoparticles, as the optical absorption cross-section and catalytic activity of the nanoparticles are highly sensitive to their size, structure, and composition. One of the techniques developed for tuning the size distribution of colloidal nanoparticles to the needs of practical applications is the laser fragmentation in liquid (LFL) [10-18], where short pulse laser irradiation of a colloidal solution is used to fragment larger nanoparticles and produce a population of smaller nanoparticles with a narrow size distribution. This method is particularly suitable for post-processing of nanoparticles generated by pulsed laser ablation in liquid (PLAL) [8,19-21], a highly effective and robust technique that, however, often produces rather broad and even bimodal nanoparticle size distributions [22-24]. The LFL not only provides a cost-effective alternative to other post-processing techniques, such as centrifugation or salinity size quenching, but is also uniquely suited for the synthesis of ultrasmall nanoparticles with diameters below 5 nm [16-19] and sub-nanometer atomic clusters [25], which have a high potential for catalysis [26,27].

The practical importance of LFL has stimulated experimental and theoretical efforts to reveal the mechanisms responsible for nanoparticle fragmentation, as reviewed in refs. [14,19,21]. Experimentally, indirect information on the mechanisms is obtained through analysis of changes in the nanoparticle size distribution [10,12,13,16-18], as well as from the results of time-resolved X-ray [28,29] and optical [29-31] probing of the dynamics of nanobubbles generated around the irradiated nanoparticles. The fragmentation process itself, usually assumed to occur inside the nanobubbles, has largely remained out of reach for the direct experimental probing. Only recently, first insights into the fragmentation dynamics and the evolution of the fragmentation products were provided by the results of *in situ* X-ray probing of LFL of Au nanoparticles [17].

While the translation of the experimental observations to the mechanistic understanding of LFL can be facilitated by computational modeling, most of the hydrodynamic [32-35] and atomistic simulations [36-38] performed so far have been focused on the analysis of the heat transfer and nanobubble formation around nanoparticles that do not experience disintegration. The transition to the nanoparticle fragmentation regime brings the complexity of the computational treatment of the problem to the level that has largely been out of reach for the existing computational models.

The recent development of a new computational model combining an atomistic molecular dynamics (MD) simulation of laser interaction with a metal nanoparticle, a continuum-level treatment of size-dependent electron-phonon coupling in the nanoparticle and nanoparticle fragments, and a coarse-grained MD representation of liquid environment [39] has enabled detailed computational investigation of LFL on a timescale that exceeds that of the evolution of a nanobubble generated around the nanoparticle. The first MD simulation of LFL was performed for a 20 nm Au nanoparticle irradiated by a 10 ps laser pulse in water at a deposited energy density comparable to that required for complete vaporization of the nanoparticle. The simulation revealed a complex picture of the nanoparticle fragmentation proceeding through an explosive decomposition of the irradiated nanoparticle into vapor, atomic clusters and small droplets, prompt injection of the phase explosion products into the water environment beyond the boundary of the expanding nanobubble, rapid quenching, solidification, and aggregation of the nanoparticle fragments occurring at the timescale of the nanobubble collapse. The results of the first simulation demonstrate the ability of the model to provide insights into the mechanisms of LFL and motivate an extension of the modeling effort to explore the effect of irradiation parameters on the fragmentation dynamics and the characteristics of the fragmentation products.

In this paper, we report the results of three additional simulations of LFL of a Au nanoparticle aimed at establishing the dependence of the fragmentation mechanisms on the energy density deposited by the laser pulse. The simulations reveal that the decrease of the energy density from 80% of the energy required to fully vaporize the Au nanoparticle [39] down to 60% and 40% of the vaporization energy leads to qualitative changes in the fragmentation mechanisms. In contrast to the explosive fragmentation and prompt injection of all of the fragmentation products into water surrounding the nanobubble observed at the high energy density [39], a substantial fraction of the nanoparticle material end up inside the nanobubble at lower energy densities, and the fragmentation produces a large central fragment surrounded by smaller satellite fragments. The origin and size of the central and satellite fragments are rather dissimilar in the two energy density regimes considered in the present paper, which reflects the existence of two distinct low-energy fragmentation mechanisms revealed in the simulations.

2 Computational model

The simulations of LFL of a 20 nm Au nanoparticle irradiated in water by a 10 ps laser pulse are performed with a computational model developed in ref. [39] and schematically illustrated in Figure 1. The Au nanoparticle is located in the center of a spherical computational domain and is surrounded by water. The laser-induced processes in the nanoparticle are simulated with an atomistic model combining the classical MD method with a continuum treatment of the laser energy deposition and electron-phonon coupling inspired by the two-temperature model (TTM) [40,41]. The water environment is represented by a coarse-grained (CG) MD model, where the degrees of freedom missing in the CG

representation of water are accounted for through a heat bath approach that associates an internal energy variable with each CG particle [42-45]. The spherical pressure waves emitted from the irradiated nanoparticles propagate away from the computational domain through a nonreflecting boundary condition [46,47] adapted for the spherical geometry of the problem. A detailed description of the computational model is given in ref. [39], and below we only provide the parameters specific for the simulations reported in this paper.

The simulations are performed for a 20 nm Au nanoparticle consisting of 240865 atoms. The interactions between Au atoms are described by the embedded atom method (EAM) potential with parametrization suggested by Zhakhovskii et al. [48]. The CG water shell surrounding the Au nanoparticle has a thickness of 50 nm and consists of about 11 million CG particles. This thickness of the water shell is sufficiently large to ensure that all products of the laser fragmentation remain within the computational domain during the simulations. The laser irradiation is simulated through a source term added to the TTM equation for the electron temperature. The source term simulates the excitation of the conduction-band electrons by a laser pulse with a Gaussian temporal profile and a full width at half maximum pulse duration of 10 ps. Since the size of the nanoparticle is smaller than the mean free path of the excited electrons (~100 nm in Au [49]), the laser energy is deposited uniformly within the nanoparticle. The simulation starts 25 ps before the time when the 10 ps laser pulse reaches its peak power to ensure the complete laser energy deposition to the nanoparticle.

The range of energy densities deposited by the laser pulse considered in the simulations is chosen to cover the distinct mechanisms of laser-induced fragmentation of Au nanoparticles, from the laser melting and evaporation at 1.2 and 1.8 eV/atom to the fragmentation followed by a partial rebound of the fragmentation products from the boundary of the nanobubble at 2.7 eV/atom, and to the prompt injection of all fragmentation products into a shell-like water region outside the boundary of the nanobubble at 3.6 eV/atom. The results for 3.6 eV/atom are reported elsewhere [39], and in this paper we focus on the two simulations performed at 1.8 and 2.7 eV/atom. These simulations represent two different mechanisms of LFL that have not yet been investigated in the simulations or discussed in the literature.

The values of laser fluence that correspond to the deposited energy densities used in the simulations can be obtained based on Mie theory calculation of the absorption efficiency (ratio of the absorption cross-section to the particle cross-section), which is found to be 1.228 for a 20 nm Au nanoparticle irradiated at a wavelength of 532 nm in water [39]. With this absorption efficiency, the incident laser fluences corresponding to the absorbed energy densities of 1.8 and 2.7 eV/atom are 180 and 270 J/m^2, respectively. We note, however, that the Mie theory calculations have been reported to result in a significant overestimation of the energy density in the regime of LFL [17,39].

To provide a reference scale for the energy density deposited by the laser pulse, the values of energy density required for inducing the phase transformations in bulk Au by slow heating, when the material remains in the state of thermodynamic equilibrium at 1 atm pressure, are shown on the right side of Figure 1. The integration of temperature dependent heat capacity of Au [50] from 300 K to the melting temperature of T_m = 1337 K yields an energy density of 29.1 kJ/mol (0.30 eV/atom). By adding the enthalpy of melting, ΔH_m = 12.72 kJ/mol = 0.13 eV/atom, we obtain 0.43 eV/atom for complete melting of Au at T_m. Further heating of molten Au from T_m to the boiling temperature of T_b = 3131 K requires an energy density of 59.1 kJ/mol (0.61 eV/atom), and the complete vaporization at T_b adds the heat of vaporization, ΔH_v = 331.0 kJ/mol = 3.43 eV/atom [50]. The total energy required for the complete vaporization of Au under conditions of slow/equilibrium heating starting from the room temperature is 4.48 eV/atom. The cohesive energy of Au, E_c = 368.4 kJ/mol = 3.82 eV/atom [50], is also marked on the energy scale in Figure 1, since the cohesive energy is often used as a reference energy level in theoretical and computational studies of laser fragmentation of nanoparticles, e.g., refs. [51-53].

While the values of energy density listed above are evaluated based on the experimental properties of Au [50], the EAM potential used in the present study [48] provides a good quantitative description of experimental properties of Au, including the melting temperature T_m^{EAM} = 1330 K, enthalpy of melting ΔH_m^{EAM}= 0.13 eV/atom, and cohesive energy E_c^{EAM}= 367.6 kJ/mol = 3.81 eV/atom. The heat capacity of the model Au represented by the combined TTM-MD model includes the temperature-dependent vibrational and electronic contributions, with the total value ranging from 25.4 J mol^{-1} K^{-1} at 300 K to 31.3 J mol^{-1} K^{-1} at T_m^{EAM}, which is close to the experimental range of 25.3 J mol^{-1} K^{-1} at 300 K to 32.3 J mol^{-1} K^{-1} at T_m [50].

3 Results and discussion

The conditions of the simulations of LFL discussed in this paper were selected based on the results of a series of preliminary simulations that suggested the existence of two distinct mechanisms of the nanoparticle fragmentation leading to the formation of a large central fragment surrounded by smaller satellite fragments. The first mechanism, where the large fragment is generated by a partial rebound of the fragmentation products from the boundary of the nano-

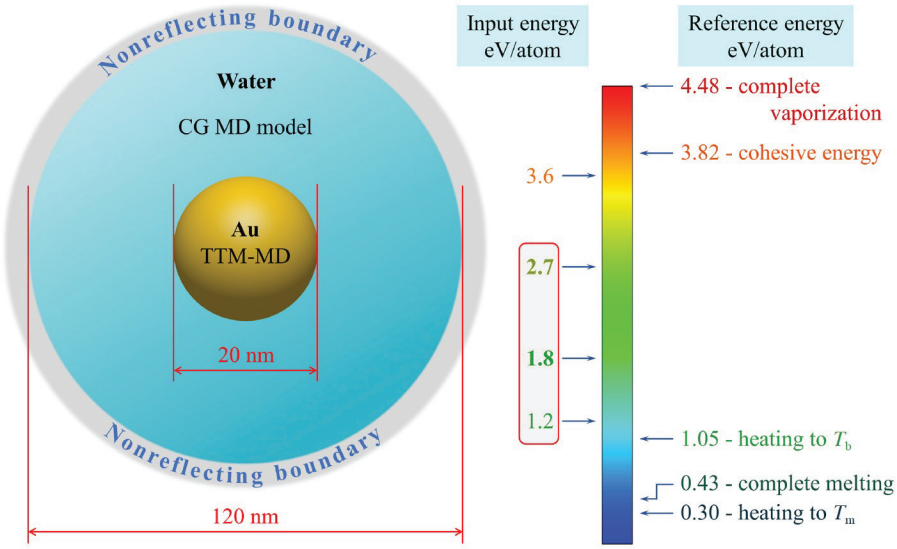

Figure 1 (Color online) Schematic representation of the computation setup. A Au nanoparticle with an initial diameter of 20 nm is immersed in a water environment and irradiated by a 10 ps laser pulse. The laser excitation and fragmentation of the nanoparticle are simulated with the atomistic TTM-MD model. A 50-nm-thick shell of water surrounding the nanoparticle is represented by the CG MD model. The acoustic impedance matching pressure-transmitting boundary condition ensures nonreflecting propagation of the laser-induced spherical pressure wave away from the computational domain. The values of the energy density deposited by the laser pulse in the simulations of LFL, along with the reference energy levels required for heating, melting and vaporization of bulk Au material are marked on the energy density scale shown on the right side of the figure. The red rectangle outlines the energy densities used in the simulations discussed in the present paper.

bubble, is illustrated by a simulation performed at a deposited energy density of 2.7 eV/atom and is discussed first, in sects. 3.1 and 3.2. The second mechanism, where small satellite clusters are nucleating from atoms that evaporate from the surface of the irradiated nanoparticle and end up in a thin water layer surrounding the transient laser-induced nanobubble, is exemplified by a simulation performed at an energy density of 1.8 eV/atom and is discussed in sect. 3.3.

3.1 Fragmentation at 2.7 eV/atom: "Mild" phase explosion and partial rebound from the surface of nanobubble

The energy density deposited by the laser pulse in the simulation discussed in this subsection, 2.7 eV/atom, is roughly in the middle between the energy needed to heat the nanoparticle to its boiling temperature T_b and that required for complete vaporization of the nanoparticle at T_b (see Figure 1). The heating of the nanoparticle by the 10-ps laser pulse, however, is too fast for any significant evaporation to occur as the nanoparticle is superheated up to the level approaching the thermodynamic critical temperature, when the release of vapor proceeds in an explosive manner [54-56] and leads to a rapid disintegration of the nanoparticle. In contrast to the simulation performed at a higher energy density of 3.6 eV/atom [39], where the deposited energy density is significantly above the threshold for the phase explosion, and the nanoparticle promptly disintegrates into vapor and small fragments, the energy density deposited in the present simulation is close to the threshold for the phase explosion. As a result, the phase decomposition is less vigorous (thus, referred to as a "mild" phase explosion in the discussion) and proceeds through several stages that can be identified from the snapshots shown in Figure 2, as well as from the pressure and density contour plots shown in Figure 3.

As can be seen from Figure 3(a), the phase explosion of the superheated nanoparticle creates a large pressure in excess of 500 MPa by the time of ~25 ps, which corresponds to the time when the 10 ps laser pulse reaches its peak power. The relaxation of this pressure proceeds through the expansion and eventual disintegration of the nanoparticle, which in turn leads to the generation of a spherical pressure pulse that propagates through the water environment and leaves the computation domain through the spherical pressure-transmitting boundary with minimal reflection. The initial evolution of the pressure pulse is additionally illustrated by the profiles shown in Figure 4 for three moments of time. The profiles of the laser-induced pressure pulse have shapes similar to those predicted in continuum-level simulations performed below the nanoparticle fragmentation threshold [32,35]. Two notable differences, however, are a substantially larger, in excess of 150 MPa, initial amplitude of the pressure pulse and a shorter duration/spatial extent of the pulse—only about 20 nm in Figure 4 as compared with about 100 [35] and 40 nm [32] for 50 nm Au nanoparticles irradiated by 10 and 200 fs laser pulses, respectively. The larger initial amplitude also leads to a faster decay of the pressure

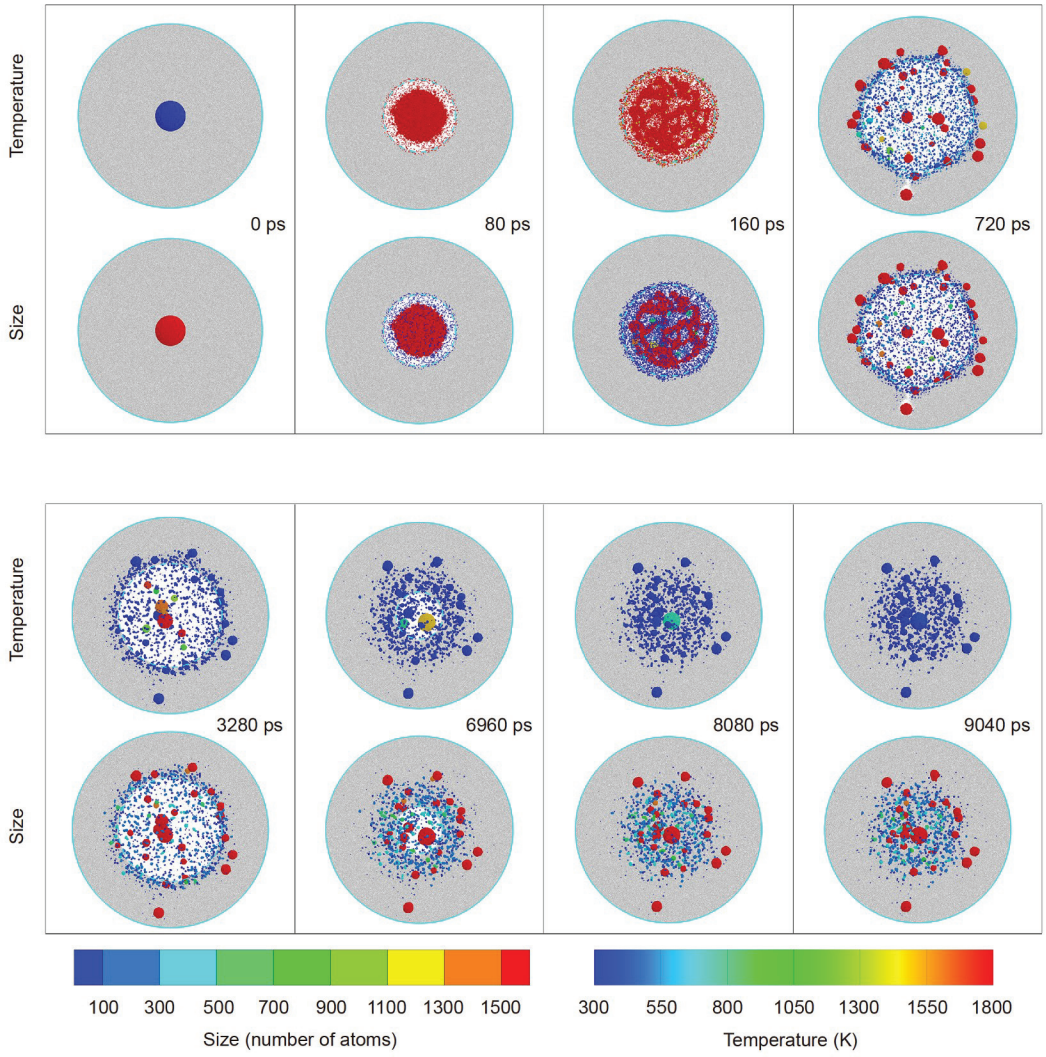

Figure 2 (Color online) Atomistic snapshots from a simulation of LFL of a 20 nm Au nanoparticle irradiated by a 10 ps laser pulse at a deposited energy density of 2.7 eV/atom. All of the Au atoms are shown in the snapshots and are colored by the average temperature (upper rows) and size (lower rows) of the clusters or nanoparticles they belong to. The representation of the water environment is limited to middle 2-nm-thick slices cut from the central parts of the systems, where the CG water particles are represented by gray dots. In order to provide a clear picture of the fragmentation process, the images of Au atoms are superimposed on top of the slices of water particles shown in the background. The solid light blue circles outline the computational domain and mark the region where the nonreflecting boundary condition is applied. The dashed light blue circles show the boundary of the laser-induced nanobubble.

pulse amplitude P_a with the radial distance r traveled by the pulse. The initial scaling of the pressure pulse amplitude is approximately $P_a \propto r^{-2}$, as shown by the dashed line in Figure 4. This scaling is stronger than $P_a \propto r^{-1}$ expected for the spherical spreading of the pressure pulse energy in the absence of the dissipation and radial broadening of the pulse. It is also stronger than $P_a \propto r^{-1.5}$ scaling observed in continuum simulations of weaker stress pulses [35], but matches the decay rate characteristic of laser-generated spherical shock waves [57,58].

The rapid evaporation of Au atoms from the surface of the nanoparticle contributes significantly to the energy transfer from the nanoparticle to the surrounding water and drives the formation and expansion of a nanobubble, which reaches the radius of 24 nm by 80 ps, 35 nm by 300 ps, and slowly expands further to reach the maximum radius of 37 nm by 1 ns. Simultaneously, the internal release of Au vapor drives the expansion and decomposition of the superheated nanoparticle into a network of interconnected regions of molten Au arranged into a gradually expanding shell-like structure. While the shell-like nature of the distribution of the liquid regions may not be apparent from the snapshots shown for 80 and 160 ps in Figure 2 where three-dimensional views of all Au atoms are presented, it can be clearly seen from the density contour plot in Figure 3(c). The high-density region that corresponds to the liquid shell appears by about 70 ps, gradually evolves into a continuous network of liquid regions (e.g., see the snapshot at 160 ps in Figure 2), and de-

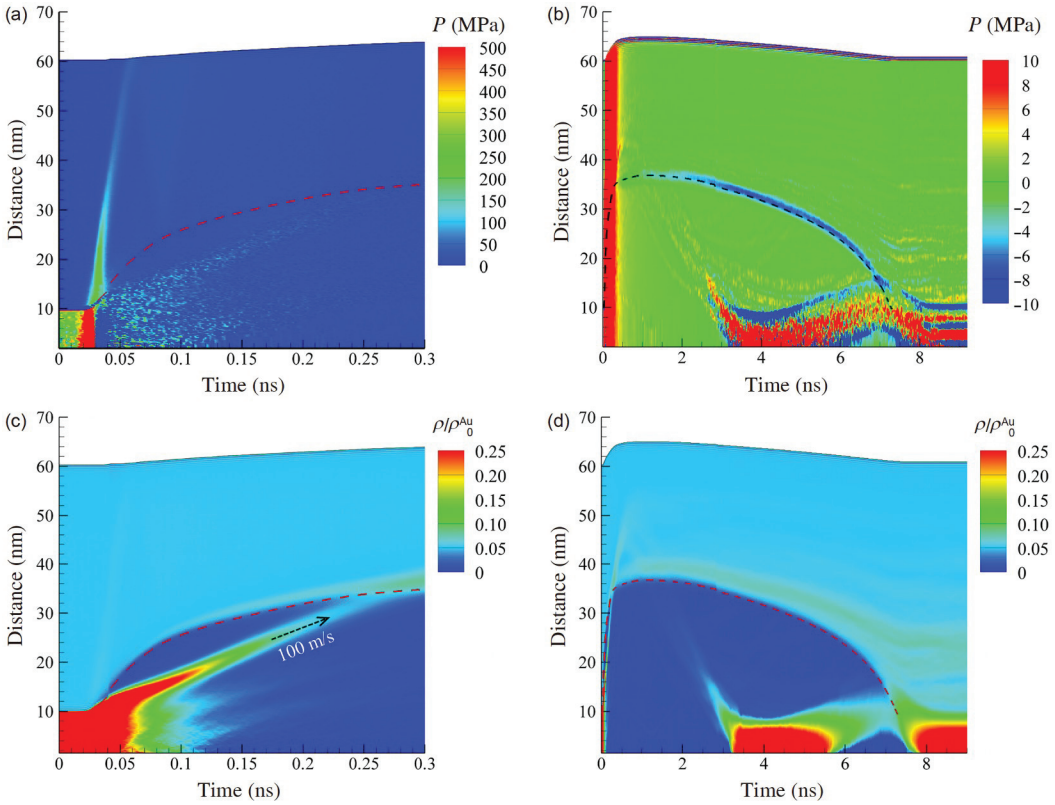

Figure 3 (Color online) Contour plots showing the evolution of pressure ((a), (b)) and density ((c), (d)) in a simulation of LFL of a 20 nm Au nanoparticle irradiated by a 10 ps laser pulse at a deposited energy density of 2.7 eV/atom. The left panels illustrate the initial stage of the fragmentation (up to 300 ps), and the right panels show the evolution of pressure and density until the end of the simulation. The density scale is normalized by the room temperature density of crystalline Au, ρ_0^{Au}. The dashed lines (red in (a), (c), (d), and black in (b)) track the motion of the nanobubble surface defined as a location where the water density is equal to 50% of the density of liquid water at room temperature. The dashed arrow in (c) marks the high-density region that corresponds to the expanding shell of molten Au produced by the explosive phase decomposition of the irradiated nanoparticle.

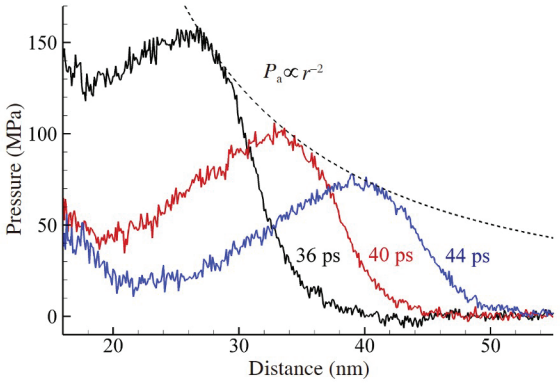

Figure 4 (Color online) Profiles of the spherical pressure wave propagating in water from a 20 nm Au nanoparticle irradiated by a 10 ps laser pulse at a deposited energy density of 2.7 eV/atom. The pressure profiles are shown for 36, 40, and 44 ps after the start of the simulation. The 10 ps laser pulse reaches its peak power at 25 ps. The dashed line outlines the decrease of the pressure pulse amplitude P_a with the radial distance r traveled by the pulse.

composes into individual droplets by ~200 ps. We note that the initial dynamics of the nanoparticle disintegration discussed above is similar to that observed in simulations of laser-induced fragmentation of molecular [59], Lennard-Jones [52] and Au [53] nanoparticles in a vacuum, where the transient appearance and disintegration of the liquid shell is also attributed to the rapid release of vapor in the nanoparticles undergoing the explosive phase decomposition.

Interestingly, the expansion velocity of the liquid shell, about 100 m/s (Figure 3(c)) is lower than the initial velocity of the nanobubble expansion. As a result, a transient gap filled with Au and water vapor appears between the expanding Au shell and the surface of the nanobubble, as can be seen from the snapshots shown in Figure 2 for 80 and 160 ps, as well as from the density contour plot in Figure 3(c), where the surface of the nanobubble is marked by the red dashed line. As the nanobubble expansion slows down, the gap closes, and the droplets produced through the disintegration of the liquid Au shell are reaching the surface of the nanobubble by the time of about 250 ps. The metal droplets are injected into water, and most of them remain immersed in water during the further expansion and collapse of the nanobubble.

Several large droplets, however, are reflected by the action of repulsive forces generated by the rapid vaporization of water that comes in contact with the hot metal droplets. These repulsive forces are of a similar nature to those responsible for the inverse Leidenfrost effect, first observed for millimeter-scale metal particles laser-heated in water and repeatedly bouncing from the walls of gas bubbles formed around them [60]. In the present simulation, the reflected droplets converge around the center of the nanobubble between 3 and 4 ns and coalesce into a single droplet. The large droplet produced by the coalescence of the fragmentation products is slowly drifting away from the center of the nanobubble during the time from about 5 to 7 ns, but is pushed back to the center by the collapsing nanobubble, as can be seen from the density contour plot shown in Figure 3(d). An additional detailed analysis of the formation of the fragmentation products is provided below, in sect. 3.2.

The generation and collapse of the nanobubble play an important role in the fragmentation process, as well as in cooling and coarsening of the fragmentation products. The evolution of the nanobubble can be clearly seen in the pressure and density contour plots, where the location of the surface of the nanobubble is marked by the dashed lines. In the pressure contour plot shown in Figure 3(b), the dashed line coincides with a narrow blue band of negative pressure related to the surface tension, which provides the main driving force for the nanobubble collapse. Using the value of the surface tension evaluated for CG water [44], γ = 0.073 J/m^2, the Laplace pressure produced by the surface of the nanobubble of radius R, $P_L = 2\gamma/R$, can be estimated to increase from about 3.9 MPa at 1 ns (R = 37 nm), to 4.6 MPa at 4 ns (R = 32 nm), and to 6.1 MPa at 6 ns (R = 24 nm). All these values of P_L are substantially larger than the difference between the pressure inside and outside the nanobubble, leading to the rapidly accelerating nanobubble collapse.

Another prominent feature of the pressure contour plot in Figure 3(b) is the presence of negative and positive pressure stripes that appear inside the nanobubble at around 1 ns and remain in the central part of the system after the nanobubble collapse. This pressure variation is related to the tension at the surface of large metal droplets balanced by the compression in the interior of the droplets. As discussed above, these droplets reflect from the boundary of the nanobubble, move toward the center of the nanobubble, and coalesce into a large core nanoparticle at 3-4 ns. Note that, since the pressure and density in the contour plots are calculated by averaging over spherical shells that include both water and Au particles, the relative contribution of the Au particles increases as they move toward the center of the system. In particular, the increase of the density and pressure in the central part of the system at around 4-5 ns corresponds to the large metal droplet passing through the center of the system. As the droplet drifts away from the center after 5 ns, the density and pressure in the center decrease again, until the droplet is pushed back to the center by the collapsing nanobubble at about 7.5 ns.

The interplay of the fragmentation process and the nanobubble dynamics can be further illustrated by considering the evolution of the water and Au density profiles shown in Figure 5. The profiles plotted for 80 ps show that the initial expansion of the nanobubble is faster than that of the shell-like transient structure of interconnected regions of molten gold. We can also see that some of the Au atoms and atomic clusters are already implanted into the water environment at this early time. As discussed above, this injection of the hot metal vapor into the water is one of the main driving forces behind the rapid expansion of the nanobubble. As the nanobubble expansion slows down, the droplets produced through the decomposition of the liquid Au shell are getting in contact with the surface of the nanobubble (profiles at 300 ps). Many of these droplets are injected as deep as 15 nm

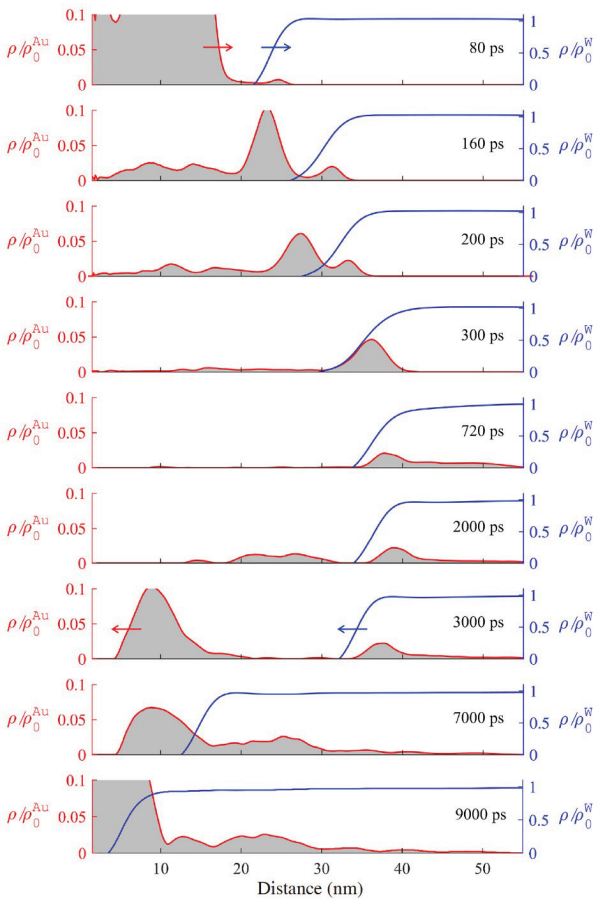

Figure 5 (Color online) Density profiles for gold (red lines outlining gray areas) and water (blue lines) plotted at different times during the simulation of LFL of a 20 nm Au nanoparticle irradiated by a 10 ps laser pulse at a deposited energy density of 2.7 eV/atom. The densities of gold and water are normalized by their respective room temperature values, ρ_0^{Au} and ρ_0^{W}. The red and blue arrows show the dominant directions of motion of gold and water, respectively. The animated sequence of the density profiles is provided in the Supporting Information.

beyond the nanobubble surface (profiles at 720 ps), but some of the largest droplets are reflected and move back toward the center of the nanobubble (profiles at 2000 and 3000 ps). Several of the reflected droplets coalesce into a large droplet that then slowly drifts off-center of the rapidly shrinking nanobubble (profiles at 7000 ps) but is pushed back to the center by the nanobubble collapse (profiles at 9000 ps).

When considering the Au density profiles, it should be noted that, similar to the contour plots, the density profiles are affected by averaging over the spherical shell regions with volumes increasing quadratically with the distance from the center of the system. Nevertheless, the virtual absence of Au inside the nanobubbles suggested by the density profiles shown for 300 and 720 ps is not an artifact of averaging over spherical shells, but reflects the injection of almost all products of the nanoparticle fragmentation into the water environment beyond the boundary of the nanobubble. The absence of Au fragments inside the nanobubble at this stage of the fragmentation process may not be apparent by viewing the corresponding snapshots in Figure 2, where three-dimensional views of all Au atoms are superimposed on thin slices of water environment.

3.2 Fragmentation at 2.7 eV/atom: Characterization of the fragmentation products

The size distribution of the atomic clusters and nanoparticles produced by LFL [10,12,13,16-18] and the internal structure (phase composition and presence of crystal defects) of the fragmentation products are of high practical interest for applications that rely on LFL for tuning the nanoparticle characteristics to the specific requirements of the applications. Therefore, in this subsection, we consider the connections between the fragmentation mechanisms discussed in the previous subsection and the evolution of the size distribution and internal structure of the fragmentation products.

The time evolution of the mass-weighted size distribution of the fragmentation products is shown in Figure 6, where the size of a cluster or a nanoparticle is expressed in terms of the equivalent diameter defined as the diameter of a spherical particle with the same number of atoms and a density of the Au crystal at 300 K [39]. A prominent feature of the size distributions is an early formation of two distinct groups of fragments generated during the first several hundreds of picoseconds after the laser irradiation, small atomic clusters and nanoparticles (smaller than 3 nm) and larger nanoparticles with sizes between 5 and 7 nm, followed by the delayed emergence of a large nanoparticle with a diameter of 11 nm at about 3.3 ns.

The first group of fragments, marked as ① in Figure 6(a), forms from the hot metal vapor rapidly released in the course of the explosive phase decomposition discussed in sect. 3.1. The vapor and atomic clusters with sizes below 1 nm account for 23% of the total mass of the fragmentation products at 200 ps (leftmost blue bar in Figure 6(b)). Most of the metal vapor and atomic clusters are promptly injected into the water environment, where the clusters grow into nanoparticles with equivalent diameters of 1 to 3 nm. By the time of 9.2 ns, these nanoparticles account for 35% of the total mass of the fragmentation products.

The second group of fragments, marked as ② in Figure 6(a), emerges from the disintegration of the transient shell-like structure of interconnected regions of molten gold produced by the explosive disintegration of the irradiated nanoparticle. Already at 250 ps, before the nanoparticles produced by the decomposition of this shell-like structure reach the surface of the nanobubble (see Figures 3(c) and 5), the nanoparticles with equivalent diameters of 5 to 8 nm account for 46% of the total mass of the fragmentation products. At 2 ns, the fragments with a narrow range of diameters of 6 to 7 nm account for 35% of the total mass of the fragmentation products.

The third type of fragmentation products, marked as ③ in

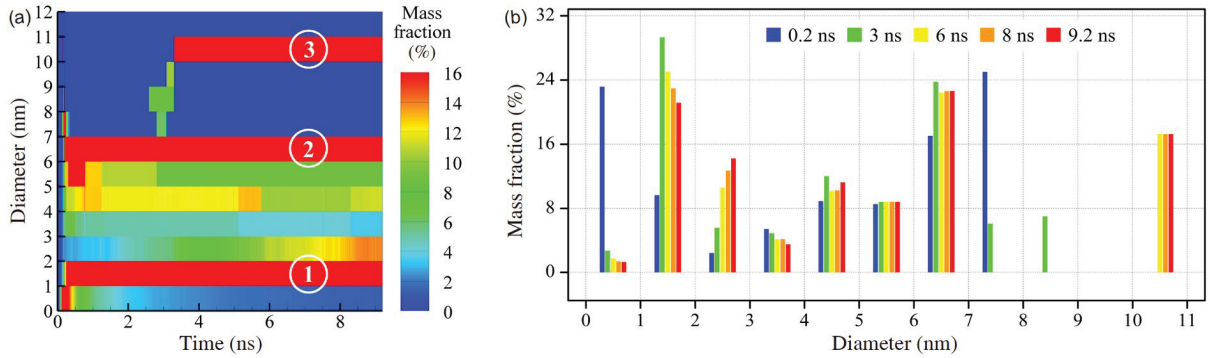

Figure 6 (Color online) The evolution of the mass-weighted size distribution of the fragmentation products predicted in a simulation of LFL of a 20 nm Au nanoparticle irradiated by a 10 ps laser pulse at a deposited energy density of 2.7 eV/atom. The mass fraction of nanoparticles with diameters that fall within the bins with the width of 1 nm is calculated and shown as a function of time in (a) and in the form of histograms plotted for five moments of time and colored by time in (b). For any given time, the sum over all bins is equal to 100%. The encircled numbers in (a) mark the three dominant groups of nanoparticles emerging from the fragmentation process.

Figure 6(a), is represented by a large nanoparticle formed at about 3.3 ns through the coalescence of several large droplets reflected from the surface of the nanobubble due to the nanoscale inverse Leidenfrost effect discussed above, in sect. 3.1. The single fragment generated inside the evolving nanobubble accounts for more than 17% of the total mass of the fragmentation products and has an equivalent diameter of about 11 nm. This fragment stays close to the center of the system after the nanobubble collapse at about 7.5 ns and does not undergo any significant changes in its size after the time of its formation at 3.3 ns.

The origin of the first two groups of the nanoparticles (① and ②) can be related to the two channels of the nanoparticle formation observed in a simulation performed at a higher deposited energy of 3.6 eV/atom [39], where both the growth of small nanoparticles from vaporized metal atoms and the direct injection of compact nanodroplets propelled by the phase explosion into the water environment was observed. The notable differences include a much larger initial fraction of the vaporized gold and substantially smaller sizes of the nanoparticles produced by the second channel (direct injection of nanoparticles into water) at the higher deposited energy. Indeed, the nanoparticles generated at 3.6 eV/atom remain below 4 nm until the end of the simulation at 14.5 ns [39], while most of the nanoparticles generated through the channel ② at 2.7 eV/atom have diameters of 6 to 7 nm.

The third mechanism of the nanoparticle generation, denoted as ③ in Figure 6(a), has not been discussed in the literature so far. Therefore, we perform an additional analysis of this mechanism by considering the trajectories of all atoms that end up in the largest nanoparticle formed inside the nanobubble. The part of the atomic trajectories shown in Figure 7(a) corresponds to the explosive fragmentation of the initial nanoparticle that, among other fragmentation products, generates several droplets that eventually contribute to the central nanoparticle. These droplets originate from the shell-like structure of interconnected liquid regions, as can be seen from the radially extended distributions of the atoms that form the droplets at 160 and 240 ps (colored with two shadows of green in Figure 7(a)). The droplets cross the surface of the nanobubble by about 300 ps and are all found inside the liquid environment, beyond the boundary of the nanobubble, at 480 ps. This can be seen from the locations of the red parts of the trajectories with respect to the red dashed circle in Figure 7(a). The asymmetry of the pressure exerted by water vaporized in the vicinity of the hot metal droplets (inverse Leidenfrost effect) pushes the droplets back towards the center of the nanobubble, as can be seen from the trajectories shown in Figure 7(b). Some of the droplets coalesce on their way towards the center of the nanobubble, and all the reflected droplets reunite in the middle of the nanobubble at around 3.3 ns. The coalesced single nanoparticle then slowly drifts away from the center during the following several nanoseconds, and is pushed back to the center by the collapsing nanobubble at about 7.5 ns.

The contributions of the three distinct channels of the

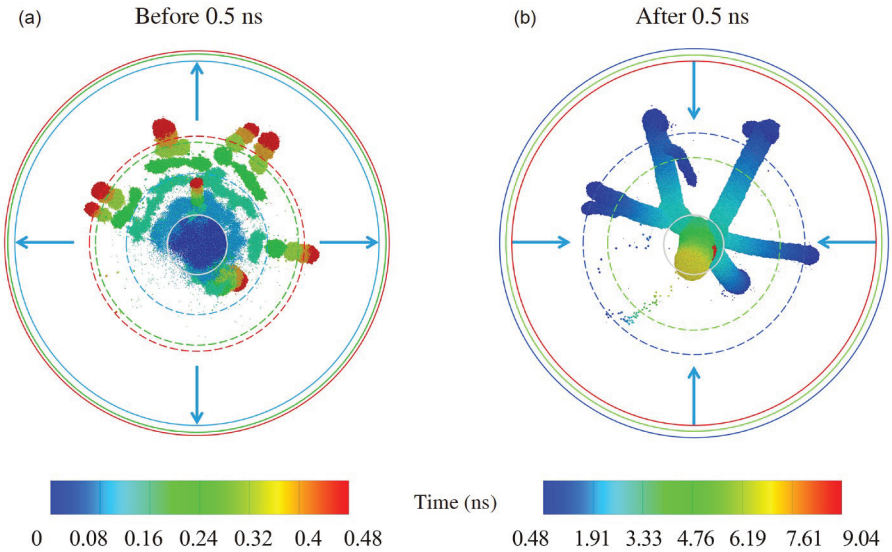

Figure 7 (Color online) Atomic trajectories of all atoms that contribute to the formation of the largest (41493 atoms) nanoparticle generated in the simulation of LFL of a 20 nm Au nanoparticle irradiated by a 10 ps laser pulse at a deposited energy density of 2.7 eV/atom. This nanoparticle is marked by ③ in the size distribution shown in Figure 6(a). The initial stage of the fragmentation process is illustrated in (a) by seven overlapping snapshots shown with time intervals of 80 ps from 0 to 480 ps and colored by time, from blue to red. The following reflection of the fragmentation products from the boundary of the nanobubble and coalescence into a single nanoparticle in the middle of the system is illustrated in (b), where the atoms in the overlapping snapshots are plotted from 480 ps to 9.04 ns, with time intervals of 80 ps before 2.8 ns, and 160 ps between 2.8 and 9.04 ns. The initial location of the 20 nm Au nanoparticle is marked by the light gray circles. The surface of the nanobubble and the position of the nonreflecting boundary are marked by the dashed and solid circles, respectively. These circles are colored by time according to the color scales used in the corresponding panels: 80 ps (blue), 240 ps (green), and 480 ps (red) in (a) and 960 ps (blue), 5040 ps (green), and 9040 ps (red) in (b).

formation of the fragmentation products identified in the simulation of LFL discussed above can be expected to affect the size distribution of the fragmentation products. Indeed, the mass-weighted size distribution at the end of the simulation, shown by red bars in the histogram plotted in Figure 6(b), has three distinct peaks at 1-2, 5-7, and 11 nm. This trimodal size distribution can be related to the results of recent time-resolved probing of the fragmentation products in small-angle scattering experiments [17], where a similar trimodal mass-weighted nanoparticle size distribution is obtained by a reverse Monte Carlo fitting of the scattering distribution at 1 μs after the laser pulse. The LFL experiments are performed for initial nanoparticles with diameters of 54 nm, and it is possible that the largest fragments in the experimental distributions (~20 nm in diameter) could form through the mechanism ③ predicted in the simulation and illustrated by Figure 7. An alternative mechanism of the prompt generation of the large fragments, where these fragments represent the remaining cores of the initial nanoparticles experiencing partial evaporation [17], appears to be less feasible. As discussed below, in sect. 3.3, the evaporation from the surface of a nanoparticle induced by a single picosecond laser pulse is unlikely to reduce the diameter of the nanoparticle by more than a factor of two.

The internal structure of the nanoparticles generated by laser-enabled synthesis in liquids has important implications for various properties of the nanoparticles. In particular, it is recognized that the presence of crystal defects in the nanoparticles produced by laser ablation in liquids has a large effect on their catalytic activity [9,61-66]. The results of atomistic simulations of laser ablation in liquids [24,45] suggest that the nanoparticles experiencing high cooling rates in the process of their formation tend to exhibit high densities of twin boundaries and stacking faults. The quenching rates are even faster in LFL, where the fragmentation products are promptly injected into the cold liquid environment, making it possible to produce highly defected nanoparticles.

Indeed, the cross-sections of two representative nanoparticles shown in Figure 8(b) reveal the presence of multiple twin boundaries (atomic planes colored red), stacking faults (pairs of red planes), platelets of metastable hcp structure (thick red regions), and grain boundaries (layers of blue atoms inside the large nanoparticle). The generation of the crystal defects in the nanoparticles can be related to the thermal history they experience during the fragmentation process. The temperature calculated by averaging over atoms that end up in four representative nanoparticles is plotted in Figure 8(a). The nanoparticles that are injected into the cold water environment by the explosive fragmentation process and remain in the water environment during the nanobubble evolution are rapidly cooled down to the temperature of the surrounding water. This is exemplified by nanoparticles consisting of 619, 1716, and 10475 atoms, with smaller nanoparticles undergoing faster cooling.

The thermal history of the largest nanoparticle consisting of 41493 atoms, however, is different and consists of three distinct stages. First, the fragments that eventually contribute to the formation of the largest nanoparticle are also injected into the water environment and experience the rapid cooling similar to that of the other fragments. As explained above and illustrated in Figure 7(b), the fragments are reflected back and reenter the nanobubble between 1.2 and 1.7 ns (as can also be seen from the density trail of the reflected droplets in Figure 3(d)). When the droplets exit the water environment and enter the nanobubble, the cooling rate is

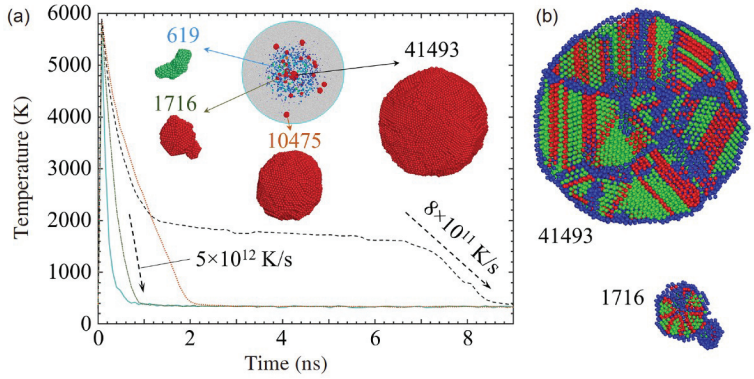

Figure 8 (Color online) The time dependence of the average temperature of atoms that end up in the four representative nanoparticles produced in the simulation of LFL of a 20 nm Au nanoparticle irradiated by a 10 ps laser pulse at a deposited energy density of 2.7 eV/atom (a) and the cross-sections of two of these nanoparticles revealing the internal defect structures (b). The inset in (a) shows enlarged views of four representative nanoparticles present in the final snapshot colored by size in Figure 2, with nanoparticles labeled by the number of atoms they consist of. The color of the temperature profiles matches that of the corresponding labels. The two dashed arrows in (a) have slopes that correspond to the cooling rates marked on the figure. The color of atoms in the cross-sections shown in (b) is chosen based on their local structural environment, so that the atoms with local face-centered cubic (fcc) and hexagonal close-packed (hcp) environments are colored green and red, respectively, while the surface atoms, grain boundaries, and other unidentified local atomic structures are colored blue. With this coloring scheme, a single red atomic plane and a pair of red planes on a green background correspond to a twin boundary and a stacking fault in the fcc structure, respectively.

dramatically reduced, and the temperature stays at an almost constant level of 1600-1800 K (20% to 35% above T_m) from 2 to 7 ns. The cooling accelerates again, and the nanoparticle is rapidly quenched when the nanobubble collapses at around 7.5 ns.

Although the 5-ns-long period of thermal insulation of the largest droplet inside the nanobubble allows for more than enough time for the droplet shape relaxation, the cooling of the spherical droplet during its solidification after the nanobubble collapse is still very rapid and proceeds with a cooling rate of about 8×10^{11} K/s. As a result, the solidification proceeds under conditions of strong undercooling and produces a nanocrystalline structure featuring high densities of stacking faults, twin boundaries, and platelets of metastable hcp structure, as can be seen in the cross-section shown for the large 41493-atom nanoparticle in Figure 8(b). The cooling rates are even higher for smaller nanoparticles quenched outside the nanobubble, which leads to the fine-grained defected structures and non-spherical shapes generated during the rapid quenching and aggregation of the small fragments, as exemplified by 619-atom and 1716-atom fragments in Figure 8.

3.3 Fragmentation at 1.8 eV/atom: Evaporation and nucleation of clusters

The reduction of energy deposited by the laser pulse down to the levels below the threshold for the phase explosion leads to qualitative changes in the fragmentation process. The fragmentation in this case takes the form of evaporation from the surface, i.e., proceeds through the heating-melting-evaporation mechanism commonly described as the main thermal fragmentation mechanism in the nanosecond pulse LFL [10,14-16]. The visual picture of this process is provided in Figure 9, where four snapshots from the simulation are shown. Similar to the simulation performed in the phase explosion regime and discussed above, the heat transfer from the hot nanoparticle to the surrounding water and the intense evaporation of Au atoms from the surface of the nanoparticle are driving the generation of a nanobubble. The nanobubble reaches its maximum radius of about 25 nm by about 150 ps after the laser pulse and then slowly shrinks during the following 3 ns.

The evolution of the nanobubble can also be seen in the pressure and density contour plots shown in Figure 10. The scale in the pressure plot in Figure 10(a) is chosen so that the tension produced at surfaces of the nanobubble and the Au nanoparticle is clearly visible. The nanobubble surface tension drives the gradual decrease in the radius of the nanobubble, which finally shrinks down to an about 2-nm-thick low-density layer adjacent to the surface of the metal nanoparticle at about 3.5 ns. The temperature of the molten nanoparticle at this time is about 3500 K (Figure 11(a)) and this temperature is sufficiently high for maintaining the steady-state low-density layer above the surface of the nanoparticle. This layer limits the heat transfer from the nanoparticle to the surrounding water. Indeed, as can be seen from the temperature plot shown in Figure 11(a), the cooling rate of the nanoparticle in the present simulation does not experience an abrupt change upon the transformation of the nanobubble into a stagnant low-density layer, and is close to 2×10^{11} K/s at the end of the simulation at 4.2 ns. This observation can be contrasted with the rapid quenching of the 41493-atom droplet after the collapse of the nanobubble, illustrated by the corresponding temperature profile in Figure 8(a), where the collapse of the nanobubble leads to a sharp increase in the cooling rate.

The processes of evaporation from the irradiated nanoparticle and condensation of the gold vapor into atomic clusters are visually represented by the snapshots shown in Figure 9 and are quantified by the time dependence of the number of evaporated atoms in Figure 11(a), as well as the

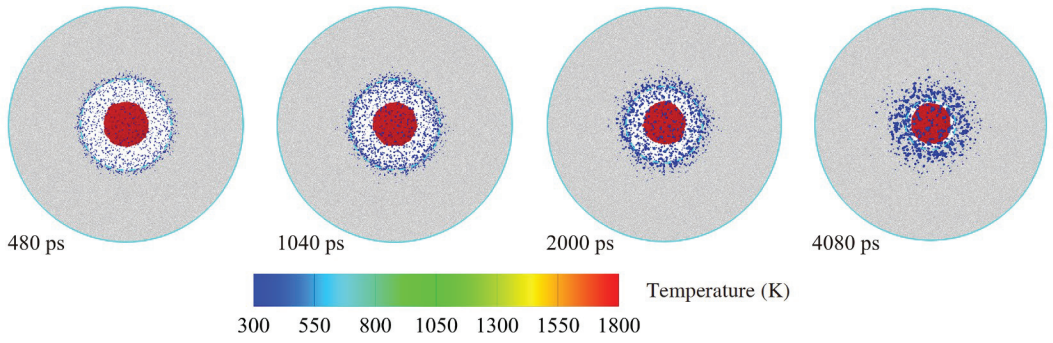

Figure 9 (Color online) Atomistic snapshots from a simulation of LFL of a 20 nm Au nanoparticle irradiated by a 10 ps laser pulse at a deposited energy density of 1.8 eV/atom. All of the Au atoms are shown in the snapshots and are colored by the average temperature of the clusters or nanoparticles they belong to. The representation of the water environment is limited to middle 2-nm-thick slices cut from the central parts of the systems, where the CG water particles are represented by small gray dots. In order to provide a clear picture of the fragmentation process, the images of Au atoms are superimposed on top of the slices of water particles shown in the background. The solid light blue circles outline the computational domain and mark the region where the nonreflecting boundary condition is applied. The dashed light blue circles show the boundary of the laser-induced nanobubble.

nanoparticle size distributions shown for 0.5 and 4 ns in Figure 11(b). The evaporated atoms enter the water surrounding the nanobubble, rapidly cool down, and condense into clusters, which further evolve into small satellite nanoparticles through the aggregation and further absorption of Au atoms. The diameters of the satellite nanoparticles remain below 2.5 nm at the end of the simulation, Figure 11(b). These satellite nanoparticles are mostly located within a 10-nm-wide water shell surrounding the main core nanoparticle, as can be seen from the density contour plot in Figure 10(b). The high rate of the initial growth of atomic clusters into the nanoparticles, observed in both the heating-melting-evaporation regime (Figure 11(b)) and the phase explosion regime (Figure 6(b)), suggests that the selection of type and concentration of surface-active species capable of preventing the growth of atomic clusters and coarsening of the nanoparticles [17,67-69] should account for the fast kinetics of the initial evolution of the size distribution in the absence of the stabilizing agents.

As the temperature of the core nanoparticle decreases, the evaporation of Au atoms slows down and almost ceases by the end of the simulation, as can be seen from Figure 11(a). The number of atoms lost by the irradiated nanoparticle by 4.2 ns due to the evaporation is 38853, and more than half of these atoms are evaporated during the first nanosecond of the simulation. The evaporation, thus, reduces the mass of the nanoparticle by about 16%, and the corresponding reduction of the nanoparticle diameter is less than 6%. These simulation results are consistent with the gradual decrease in the size of the initial nanoparticles and the appearance of a distinct population of small nanoparticles with increasing number of laser pulses reported for picosecond LFL of Au nanoparticles with initial diameters of 20-30 nm [12]. While the size reduction can be much more substantial in a single pulse nanosecond LFL [16], the observation of the largest fragments that are more than twice smaller than the initial

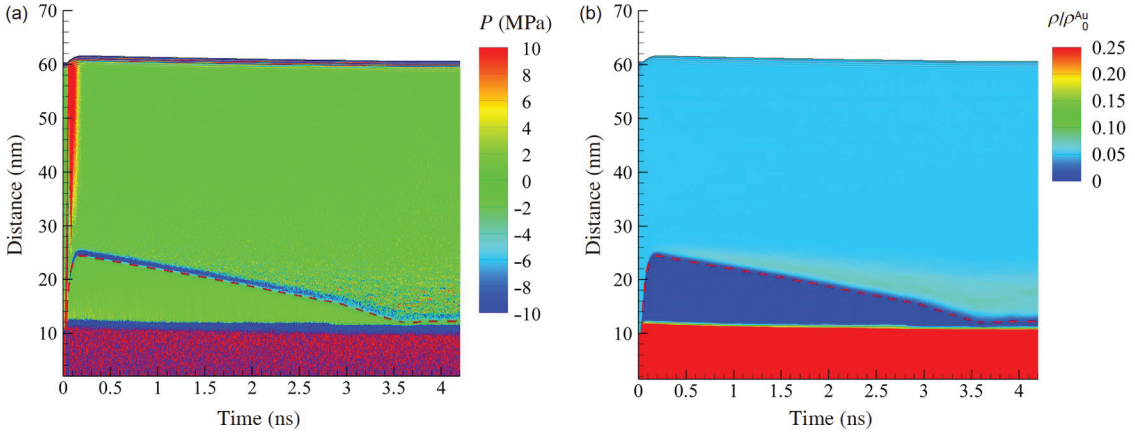

Figure 10 (Color online) Contour plots showing the evolution of pressure (a) and density (b) in a simulation of LFL of a 20 nm Au nanoparticle irradiated by a 10 ps laser pulse at a deposited energy density of 1.8 eV/atom. The density scale is normalized by the room temperature density of crystalline Au, ρ_0^{Au}. The red dashed lines mark the surface of the nanobubble defined as a location where the water density is equal to 50% of the density of liquid water at room temperature.

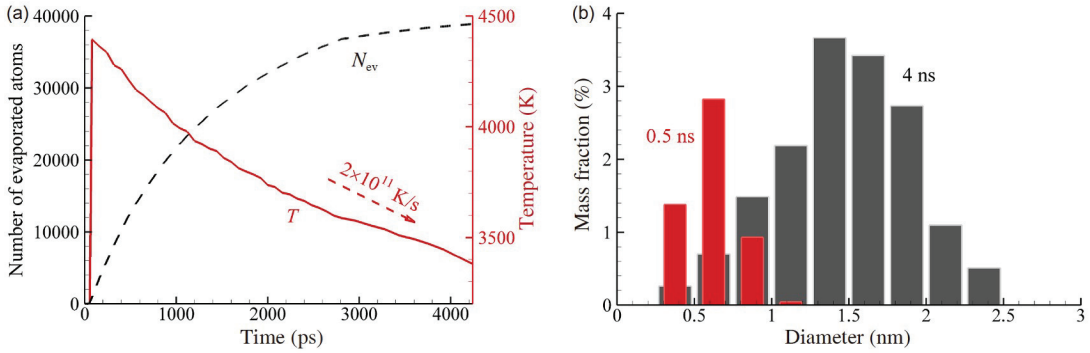

Figure 11 (Color online) The time dependence of the average temperature of the core nanoparticle, the number of evaporated atoms (a), and the nanoparticle/cluster size distribution (b) predicted in the simulation of LFL of a 20 nm Au nanoparticle irradiated by a 10 ps laser pulse at a deposited energy density of 1.8 eV/atom. The dashed arrow in (a) has a slope that corresponds to the cooling rate marked on the figure. The averaging in the calculation of temperature does not include the evaporated atoms. In (b), the mass fraction of clusters/nanoparticles of different sizes is defined with respect to the total mass of Au in the initial nanoparticle, i.e., the sum over all bins is equal to the fraction of mass lost by the core nanoparticle. The red and gray bins show the distributions at 0.5 and 4 ns, respectively.

54 nm nanoparticle in the picosecond LFL [17] is likely to indicate that the irradiation conditions in ref. [17] correspond to the explosive phase decomposition of the nanoparticle (similar to that discussed in sects. 3.1 and 3.2) rather than the heating-melting-evaporation process. Indeed, the results of the simulations suggest that a single picosecond pulse irradiation below the threshold for the phase explosion can only produce a moderate reduction of the nanoparticle diameter.

Further reduction of the deposited energy density from 1.8 to 1.2 eV/atom leads to a decrease in the maximum temperature reached by the Au nanoparticle by the end of the laser pulse down to about 3300 K, which is close to the temperature of the core nanoparticle at the end of the simulation performed at 1.8 eV/atom, about 3400 K at 4.2 ns. As a result, the evaporation is much less intense at 1.2 eV/atom, and the number of atoms evaporated by the end of the simulation at 1.3 ns, when the temperature decreases down to 2900 K, is only 474. This corresponds to a less than 0.2% decrease in the number of atoms in the core nanoparticle and a negligible decrease in the radius of the nanoparticle. The virtual absence of the energy transfer to the water through the evaporation of the nanoparticle makes a strong impact on the dynamics of the nanobubble, which reaches the maximum radius of about 14 nm by 100 ps, collapses by about 300 ps, and then exhibits several weaker rebounds until about 700 ps. The dynamics of the nanobubbles generated at lower energy densities, below the threshold for laser fragmentation, will be discussed in another paper.

4 Summary

The dependence of the mechanisms of the laser fragmentation of metal nanoparticles in a liquid environment on the energy density deposited by the laser pulse is investigated in TTM-MD simulations performed for 20 nm Au nanoparticles irradiated in water by 10 ps laser pulses. Three distinct regimes of LFL are established in the simulations and are schematically illustrated in Figure 12. The three regimes are characterized by different fragmentation mechanisms and size distributions of the fragmentation products. The results of a simulation performed at the highest energy density of 3.6 eV/atom (94% of the cohesive energy or 80% of the energy required for complete vaporization of the nanoparticle) are reported in an earlier publication [39] and are illustrated in the upper row of Figure 12. The rapid

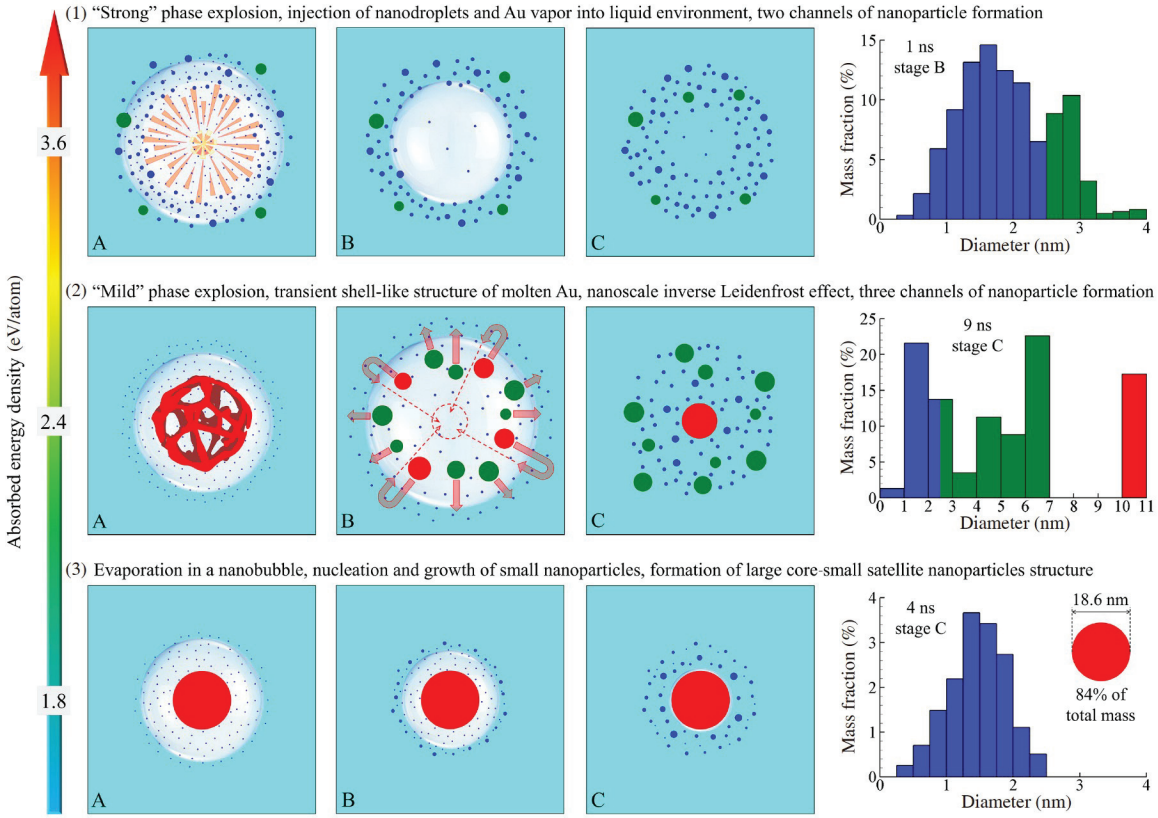

Figure 12 (Color online) Schematic representation of the three regimes of LFL revealed in the atomistic simulations: (1) "strong" phase explosion characterized by two distinct channels of the formation of the fragmentation products, (2) "mild" phase explosion characterized by three distinct channels of the formation of the fragmentation products, and (3) evaporation in the transiently formed nanobubble and condensation of the metal vapor into clusters and small satellite nanoparticles. The color of the nanoparticles in the schematics matches the color of bins in the mass-weighted size distributions shown in the right side of the figure.

energy deposition by the laser pulse rapidly melts and superheats the nanoparticle up to the limit of thermodynamic stability against an explosive phase decomposition into vapor and liquid droplets. The vigorous phase explosion drives the generation and rapid expansion of a nanobubble and leads to a prompt injection of all products of the explosive phase decomposition into water surrounding the nanobubble. Two channels of the nanoparticle formation identified at this energy density are: (1) the direct injection of compact nanodroplets into water environment followed by their rapid freezing and (2) a gradual growth of smaller nanoparticles from vaporized metal atoms. The nanoparticles formed through these two channels and the corresponding parts of the nanoparticle size distributions are colored blue and green in the first row of Figure 12.

The simulations performed at lower energy densities reveal the existence of two additional mechanisms of the nanoparticle fragmentation, with both of the mechanisms producing a large central fragment surrounded by smaller satellite fragments. The first mechanism is observed at a deposited energy density that is approximately in the middle between the energy required for heating the nanoparticle up to its boiling temperature T_b and the energy required for complete vaporization of the nanoparticle at T_b. In contrast to the "strong" phase explosion discussed above, a less vigorous, "mild" phase explosion at the reduced energy density is observed to produce a transient network of interconnected regions of molten Au arranged into a gradually expanding shell-like structure. The initial velocity of the nanobubble expansion exceeds the velocity of the expansion of the liquid shell, which decomposes into individual liquid droplets inside the nanobubble. When the hot metal droplets are injected into water, most of them rapidly cool down and remain immersed in water outside the boundary of the nanobubble. Some of the large droplets, however, are reflected by the action of repulsive forces generated by the rapid vaporization of water that comes in contact with the hot metal droplets. This rebound of the metal droplets from the boundary of the nanobubble is analogous to the inverse Leidenfrost effect acting at the nanoscale. The reflected droplets converge around the center of the nanobubble at around 3-4 ns after the laser pulse, coalesce into a single droplet, and solidify only after the nanobubble collapses at about 7.5 ns. This multistep mechanism of LFL, involving a partial reflection of the fragmentation products from the surface of the evolving nanobubble and the coalescence of the reflected fragments into a central core nanoparticle surrounded by smaller satellite fragments, has not been, to our knowledge, discussed in literature so far, and is revealed in the simulation reported in this paper.

The coexistence of three distinct channels of the nanoparticle formation in the regime of "mild" phase explosion leads to the generation of a trimodal nanoparticle size distribution, as schematically illustrated in the middle row of Figure 12. Two of the three channels, which produce nanoparticles colored blue and green, can be related to those observed in the "strong" phase explosion regime, except that the fraction of small (blue) nanoparticles is smaller and the nanoparticles produced by the injection of nanodroplets into water environment (green) are substantially larger. The third channel, where a single large nanoparticle (red) is generated through the reflection of droplets from the boundary of the nanobubble, is unique to the regime of "mild" phase explosion. We note that the discovery of this new channel of the formation of large fragmentation products (e.g., 50% of the size of initial nanoparticle) challenges the established direct association of experimental observations of large fragments with the heating-melting-evaporation mechanism and suggests an alternative origin of such fragments.

The simulation performed at an energy density reduced down to a level below the threshold for the phase explosion demonstrates the transition to a fragmentation defined by an interplay of the intense evaporation from the surface of the irradiated nanoparticle and the evolution of the nanobubble. This fragmentation regime is illustrated in the bottom row of Figure 12. The evaporation from the nanoparticle is the key factor responsible for the initial nanobubble expansion and the relatively slow decrease in the radius of the nanobubble. The evaporated atoms are absorbed by water surrounding the nanobubble, where they rapidly condense into clusters and small satellite nanoparticles. The size distribution of the satellite particles (blue in the bottom row of Figure 12) remains relatively narrow and unimodal as the nanoparticles/clusters formed from vaporized metal atoms are slowly coarsening due to the agglomeration and coalescence.

While the formation of a core-satellite structure of the fragmentation products is observed in both the evaporation regime and "mild" phase explosion regime, the size of the core produced in the two regimes is rather different. In particular, the single pulse picosecond laser irradiation in the evaporation regime is found to reduce the nanoparticle diameter by less than 6%, whereas the central core fragment generated through the coalescence of droplets reflected from the boundary of the nanobubble in the phase explosion regime has a diameter about twice smaller than the diameter of the initial nanoparticle. The computational predictions on the size of the largest fragment and the contribution of three distinct channels of the formation of the fragmentation products in the "mild" phase explosion regime are in good agreement with the trimodal mass-weighted nanoparticle size distribution observed experimentally in a recent time-resolved study of the picosecond LFL of Au nanoparticles.

The analysis of the thermal history of the fragmentation products predicted in the simulations suggests that the quenching rate can be as high as 5×10^{12} K/s for the small fragments produced in the phase explosion regime, while the

cooling of the core nanoparticle in the heating-melting-evaporation regime is more than an order of magnitude slower. The high cooling rates have direct implications for the internal structure of the nanoparticles produced by LFL, with the small rapidly quenched nanoparticles exhibiting fine-grained defected structures featuring metastable phase inclusions as well as high densities of twin boundaries, stacking faults, and other defects.

Overall, the computational predictions on the dependence of the mechanisms of LFL on the energy density deposited by the laser pulse, as well as the connections established between the fragmentation mechanisms, nanoparticle size distributions, and the defect structures in the nanoparticles, have important implications for the interpretation of the results of experimental probing of the fragmentation process. More generally, the computational results can facilitate the advancement of the LFL technique guided by the insights into the processes that control the sizes, shapes and structures of the produced nanoparticles.

This work was supported by the National Science Foundation (NSF) (Grant Nos. DMR-1708486, and CMMI-1663429). Leonid V. Zhigilei also acknowledges the Mercator Fellowship at the University of Duisburg-Essen, Germany, funded by Deutsche Forschungsgemeinschaft (Grant No. BA 3580/22-1), and the Research Award of the Alexander von Humboldt Foundation. Computational support was provided by the NSF through the Extreme Science and Engineering Discovery Environment (Grant No. TGDMR110090).

Supporting Information

The supporting information is available online at phys.scichina.com and link.springer.com. It includes an animated sequence of density profiles from the simulation of LFL performed at a deposited energy density of 2.7 eV/atom and illustrated in Figure 5. The animation is provided in the animated GIF format. The supporting materials are published as submitted, without typesetting or editing. The responsibility for scientific accuracy and content remains entirely with the authors.

1 *Handbook of Nanomaterials for Industrial Applications*, edited by C. M. Hussain (Elsevier, Amsterdam, 2020).
2 M.-C. Daniel, and D. Astruc, Chem. Rev. **104**, 293 (2004).
3 S. Jendrzej, B. Gökce, M. Epple, and S. Barcikowski, ChemPhysChem **18**, 1012 (2017).
4 L. C. Kennedy, L. R. Bickford, N. A. Lewinski, A. J. Coughlin, Y. Hu, E. S. Day, J. L. West, and R. A. Drezek, Small **7**, 169 (2011).
5 D. Kim, K. Shin, S. G. Kwon, and T. Hyeon, Adv. Mater. **30**, 1802309 (2018).
6 P. K. Jain, K. S. Lee, I. H. El-Sayed, and M. A. El-Sayed, J. Phys. Chem. B **110**, 7238 (2006).
7 Special Issue on *Nanoparticles in Catalysis*, Chem. Rev. **120**, 461 (2020).
8 R. C. Forsythe, C. P. Cox, M. K. Wilsey, and A. M. Müller, Chem. Rev. **121**, 7568 (2021).
9 Z. Li, J.-Y. Fu, Y. Feng, C.-K. Dong, H. Liu, and X.-W. Du, Nat. Catal. **2**, 1107 (2019).
10 A. Takami, H. Kurita, and S. Koda, J. Phys. Chem. B **103**, 1226 (1999).
11 F. Mafuné, J.-y. Kohno, Y. Takeda, and T. Kondow, J. Phys. Chem. B **106**, 8555 (2002).
12 S. Inasawa, M. Sugiyama, and Y. Yamaguchi, J. Phys. Chem. B **109**, 9404 (2005).
13 V. Amendola, and M. Meneghetti, J. Mater. Chem. **17**, 4705 (2007).
14 S. Hashimoto, D. Werner, and T. Uwada, J. Photochem. Photobiol. C-Photochem. Rev. **13**, 28 (2012).
15 D. Werner, and S. Hashimoto, Langmuir **29**, 1295 (2013).
16 A. R. Ziefuß, S. Reichenberger, C. Rehbock, I. Chakraborty, M. Gharib, W. J. Parak, and S. Barcikowski, J. Phys. Chem. C **122**, 22125 (2018).
17 A. R. Ziefuss, S. Reich, S. Reichenberger, M. Levantino, and A. Plech, Phys. Chem. Chem. Phys. **22**, 4993 (2020).
18 O. Havelka, M. Cvek, M. Urbánek, D. Łukowiec, D. Jašíková, M. Kotek, M. Černík, V. Amendola, and R. Torres-Mendieta, Nanomaterials **11**, 1538 (2021).
19 D. Zhang, B. Gökce, and S. Barcikowski, Chem. Rev. **117**, 3990 (2017).
20 A. Kanitz, M.-R. Kalus, E. L. Gurevich, A. Ostendorf, S. Barcikowski, and D. Amans, Plasma Sources Sci. Technol. **28**, 103001 (2019).
21 V. Amendola, D. Amans, Y. Ishikawa, N. Koshizaki, S. Scirè, G. Compagnini, S. Reichenberger, and S. Barcikowski, Chem. Eur. J. **26**, 9206 (2020).
22 A. V. Kabashin, and M. Meunier, J. Appl. Phys. **94**, 7941 (2003).
23 G. Marzun, J. Nakamura, X. Zhang, S. Barcikowski, and P. Wagener, Appl. Surf. Sci. **348**, 75 (2015).
24 C. Y. Shih, R. Streubel, J. Heberle, A. Letzel, M. V. Shugaev, C. Wu, M. Schmidt, B. Gökce, S. Barcikowski, and L. V. Zhigilei, Nanoscale **10**, 6900 (2018).
25 A. R. Ziefuss, T. Steenbock, D. Benner, A. Plech, J. Göttlicher, M. Teubner, B. Grimm-Lebsanft, C. Rehbock, C. Comby-Zerbino, R. Antoine, D. Amans, I. Chakraborty, G. Bester, M. Nachev, B. Sures, M. Rübhausen, W. J. Parak, and S. Barcikowski, Adv. Mater. **33**, 2101549 (2021).
26 M. Zhou, C. Zeng, Y. Chen, S. Zhao, M. Y. Sfeir, M. Zhu, and R. Jin, Nat. Commun. **7**, 13240 (2016).
27 M. Turner, V. B. Golovko, O. P. H. Vaughan, P. Abdulkin, A. Berenguer-Murcia, M. S. Tikhov, B. F. G. Johnson, and R. M. Lambert, Nature **454**, 981 (2008).
28 A. Siems, S. A. L. Weber, J. Boneberg, and A. Plech, New J. Phys. **13**, 043018 (2011).
29 A. Plech, S. Ibrahimkutty, S. Reich, and G. Newby, Nanoscale **9**, 17284 (2017).
30 D. Werner, A. Furube, T. Okamoto, and S. Hashimoto, J. Phys. Chem. C **115**, 8503 (2011).
31 D. Lapotko, Opt. Express **17**, 2538 (2009).
32 A. N. Volkov, C. Sevilla, and L. V. Zhigilei, Appl. Surf. Sci. **253**, 6394 (2007).
33 É. Boulais, R. Lachaine, and M. Meunier, Nano Lett. **12**, 4763 (2012).
34 J. Lombard, T. Biben, and S. Merabia, J. Phys. Chem. C **121**, 15402 (2017).
35 J. Lombard, J. Lam, F. Detcheverry, T. Biben, and S. Merabia, Phys. Rev. Res. **3**, 023231 (2021), arXiv: 2105.05022.
36 S. Merabia, P. Keblinski, L. Joly, L. J. Lewis, and J.-L. Barrat, Phys. Rev. E **79**, 021404 (2009), arXiv: 0808.3160.
37 S. Merabia, S. Shenogin, L. Joly, P. Keblinski, and J.-L. Barrat, Proc. Natl. Acad. Sci. USA **106**, 15113 (2009), arXiv: 0906.0438.
38 K. Sasikumar, and P. Keblinski, J. Chem. Phys. **141**, 234508 (2014).
39 H. Huang, and L. V. Zhigilei, J. Phys. Chem. C **125**, 13413 (2021).
40 D. S. Ivanov, and L. V. Zhigilei, Phys. Rev. B **68**, 064114 (2003).
41 C. Wu, and L. V. Zhigilei, Appl. Phys. A **114**, 11 (2014).
42 M. Tabetah, A. Matei, C. Constantinescu, N. P. Mortensen, M. Dinescu, J. Schou, and L. V. Zhigilei, J. Phys. Chem. B **118**, 13290 (2014).
43 J. Zou, C. Wu, W. D. Robertson, L. V. Zhigilei, and R. J. D. Miller, J. Chem. Phys. **145**, 204202 (2016).
44 C.-Y. Shih, C. Wu, M. V. Shugaev, and L. V. Zhigilei, J. Colloid Interface Sci. **489**, 3 (2017).

45 C.-Y. Shih, M. V. Shugaev, C. Wu, and L. V. Zhigilei, J. Phys. Chem. C **121**, 16549 (2017).
46 C. Schäfer, H. M. Urbassek, L. V. Zhigilei, and B. J. Garrison, Comput. Mater. Sci. **24**, 421 (2002).
47 E. T. Karim, M. Shugaev, C. Wu, Z. Lin, R. F. Hainsey, and L. V. Zhigilei, J. Appl. Phys. **115**, 183501 (2014).
48 V. V. Zhakhovskii, N. A. Inogamov, Y. V. Petrov, S. I. Ashitkov, and K. Nishihara, Appl. Surf. Sci. **255**, 9592 (2009).
49 J. Hohlfeld, S. S. Wellershoff, J. Güdde, U. Conrad, V. Jähnke, and E. Matthias, Chem. Phys. **251**, 237 (2000).
50 J. W. Arblaster, J. Phase Equilibria Diffus. **37**, 229 (2016).
51 L. V. Zhigilei, and B. J. Garrison, Appl. Surf. Sci. **127-129**, 142 (1998).
52 R. Fahdiran, and H. M. Urbassek, Eur. Phys. J. D **69**, 35 (2015).
53 L. Delfour, and T. E. Itina, J. Phys. Chem. C **119**, 13893 (2015).
54 V. P. Skripov, *Metastable Liquids* (Wiley, New York, 1974).
55 A. Miotello, and R. Kelly, Appl. Phys. A **69**, S67 (1999).
56 B. J. Garrison, T. E. Itina, and L. V. Zhigilei, Phys. Rev. E **68**, 041501 (2003).
57 A. Vogel, S. Busch, and U. Parlitz, J. Acoust. Soc. Am. **100**, 148 (1996).
58 A. G. Doukas, and T. J. Flotte, Ultrasound Med. Biol. **22**, 151 (1996).
59 E. Leveugle, A. Sellinger, J. M. Fitz-Gerald, and L. V. Zhigilei, Phys. Rev. Lett. **98**, 216101 (2007).
60 R. S. Hall, S. J. Board, A. J. Clare, R. B. Duffey, T. S. Playle, and D. H. Poole, Nature **224**, 266 (1969).
61 D. Zhang, J. Liu, P. Li, Z. Tian, and C. Liang, ChemNanoMat **3**, 512 (2017).
62 J.-Y. Lin, C. Xi, Z. Li, Y. Feng, D.-Y. Wu, C.-K. Dong, P. Yao, H. Liu, and X.-W. Du, Chem. Commun. **55**, 3121 (2019).
63 S. Reichenberger, G. Marzun, M. Muhler, and S. Barcikowski, ChemCatChem **11**, 4489 (2019).
64 S. Dittrich, S. Kohsakowski, B. Wittek, C. Hengst, B. Gökce, S. Barcikowski, and S. Reichenberger, Nanomaterials **10**, 1582 (2020).
65 W. Huang, A. C. Johnston-Peck, T. Wolter, W. C. D. Yang, L. Xu, J. Oh, B. A. Reeves, C. Zhou, M. E. Holtz, A. A. Herzing, A. M. Lindenberg, M. Mavrikakis, and M. Cargnello, Science **373**, 1518 (2021).
66 S. Reichenberger, Sci. China-Phys. Mech. Astron. **65**, 274208 (2022).
67 J.-P. Sylvestre, S. Poulin, A. V. Kabashin, E. Sacher, M. Meunier, and J. H. T. Luong, J. Phys. Chem. B **108**, 16864 (2004).
68 A. Letzel, S. Reich, T. dos Santos Rolo, A. Kanitz, J. Hoppius, A. Rack, M. P. Olbinado, A. Ostendorf, B. Gökce, A. Plech, and S. Barcikowski, Langmuir **35**, 3038 (2019).
69 A. R. Ziefuß, S. Barcikowski, and C. Rehbock, Langmuir **35**, 6630 (2019).